Draft version May 28, 2021
Typeset using LATEX twocolumn style in AASTeX63

3-OGC: Catalog of gravitational waves from compact-binary mergers

Alexander H. Nitz,[1,2] Collin D. Capano,[1,2] Sumit Kumar,[1,2] Yi-Fan Wang (王一帆),[1,2] Shilpa Kastha,[1,2] Marlin Schäfer,[1,2] Rahul Dhurkunde,[1,2] and Miriam Cabero[3]

[1] *Max-Planck-Institut für Gravitationsphysik (Albert-Einstein-Institut), D-30167 Hannover, Germany*
[2] *Leibniz Universität Hannover, D-30167 Hannover, Germany*
[3] *Department of Physics and Astronomy, The University of British Columbia, Vancouver, BC V6T 1Z4, Canada,*

ABSTRACT

We present the third Open Gravitational-wave Catalog (3-OGC) of compact-binary coalescences, based on the analysis of the public LIGO and Virgo data from 2015 through 2019 (O1, O2, O3a). Our updated catalog includes a population of 57 observations, including four binary black hole mergers that had not previously been reported. This consists of 55 binary black hole mergers and the two binary neutron star mergers GW170817 and GW190425. We find no additional significant binary neutron star or neutron star–black hole merger events. The most confident new detection is the binary black hole merger GW190925_232845 which was observed by the LIGO Hanford and Virgo observatories with $\mathcal{P}_{\rm astro} > 0.99$; its primary and secondary component masses are $20.2^{+3.9}_{-2.5} M_\odot$ and $15.6^{+2.1}_{-2.6} M_\odot$, respectively. We estimate the parameters of all binary black hole events using an up-to-date waveform model that includes both sub-dominant harmonics and precession effects. To enable deep follow-up as our understanding of the underlying populations evolves, we make available our comprehensive catalog of events, including the sub-threshold population of candidates, and the posterior samples of our source parameter estimates.

Keywords: gravitational waves — black holes — neutron stars — compact binaries

1. INTRODUCTION

With the advent of the current generation of interferometric gravitational-wave detectors, the observation of gravitational waves from the coalescence of compact-binary mergers has become a regular and rapidly maturing component of astronomy. The Advanced LIGO (Aasi et al. 2015) and Advanced Virgo (Acernese et al. 2015) observatories have now been observing at high sensitivity since 2015 and 2017, respectively. During this period they have completed three observing runs (O1-O3). Dozens of binary black hole mergers have been reported from these observing runs, in addition to a handful of binary neutron star coalescences (Nitz et al. 2019d; Venumadhav et al. 2019a; Abbott et al. 2019b, 2020b). Notably, GW170817 remains the sole observation with unambiguous electromagnetic counterparts (Abbott et al. 2017b,a). Novel observations such as the massive GW190521 merger (Abbott et al. 2020c) are starting to challenge our models of stellar formation (Abbott et al. 2020d; Gerosa & Fishbach 2021; Edelman et al. 2021; Zevin et al. 2021) and are pushing the limits of gravitational waveform modelling (Romero-Shaw et al. 2020; Gayathri et al. 2020; Estellés et al. 2021).

In this work, we provide a comprehensive catalog of gravitational waves from the coalescence of binary neutron star (BNS), neutron star–black hole (NSBH) and binary black hole (BBH) systems based on a deep archival search for compact-binary mergers of the public LIGO and Virgo data. The previous open gravitational-wave catalog (2-OGC) searched for the signature of compact-binary mergers in the O1 and O2 observing runs. We re-analyze the entirety of the public LIGO and Virgo data comprised of O1, O2, and the recently published O3a dataset (Vallisneri et al. 2015; Abbott et al. 2021a), which covers the first half, from April 1 to October 1 of 2019, of the concluded O3 observing run. The O3 data is being released in 6-month chunks, with O3a being the first; the second half is expected in 6 months time. Included in our data release is the complete set of sub-threshold candidates in addition to posterior sam-

Corresponding author: Alexander H. Nitz
alex.nitz@aei.mpg.de

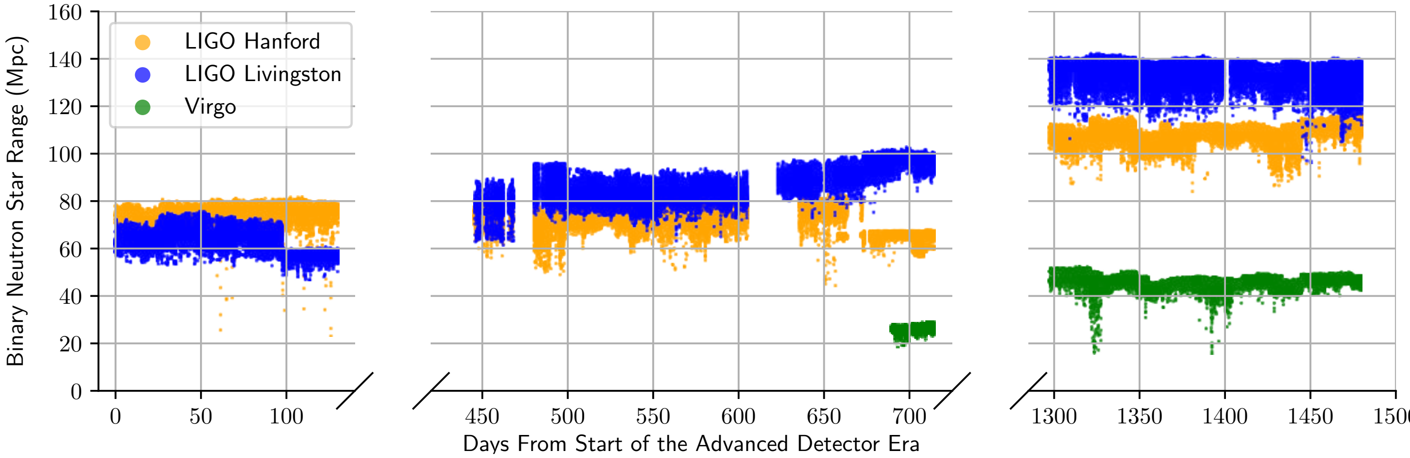

Figure 1. The sky and orientation averaged distance that a fiducial 1.4-1.4 $M_{\odot}$BNS merger can be observed by the LIGO Hanford (yellow), LIGO Livingston (blue) and Virgo (green) observatories at an SNR of 8. The O1 (left), O2 (middle) and O3a (right) observing periods are shown.

ples from estimates of the most significant mergers. Subthreshold candidates can be correlated with archival observations (e.g. from gamma-ray bursts (Burns et al. 2019; Nitz et al. 2019c), high-energy neutrinos (Countryman et al. 2019), or optical transients (Andreoni et al. 2018; Setzer et al. 2018)) to potentially uncover fainter, distant populations.

We improve the sensitivity of our analysis over our previous catalog search by targeted use of signal-consistency tests, updated data cleaning procedures, and stricter allowance for loss in signal-to-noise. As in 2-OGC, for candidates consistent with the bulk of the increasing population of observed BBH mergers, we estimate the probability of astrophysical origin using the focused BBH region of our larger search. This estimate takes into account the measured rate of mergers and the possibly confounding background noise. Additionally, for the first time in this catalog, we incorporate BNS and BBH candidates observed by a single sensitive detector using methods introduced in Nitz et al. (2020).

We find that 55 binary black hole mergers have been observed from 2015-2019 along with 2 binary neutron star mergers. These include four BBH mergers from the O3a period which had not previously been reported. Our results are broadly consistent with the cumulative sum of previous catalogs (Nitz et al. 2019a,d; Venumadhav et al. 2019a; Abbott et al. 2019b), including the recent analysis of O3a by the LVK collaboration (Abbott et al. 2020b).

2. LIGO AND VIRGO OBSERVING PERIOD

We analyze the complete set of public LIGO and Virgo data from the O1, O2, and O3a observing runs (Vallisneri et al. 2015; Abbott et al. 2021a). In our analysis, we also include data around GW170608 (Abbott et al. 2017c) and GW190814 (Abbott et al. 2020e) which were released separately (Vallisneri et al. 2015; Abbott et al. 2021a). The data sets have been calibrated by the LIGO Scientific and Virgo Collaborations to convert the optical signals at the readout ports of the interferometers into timeseries of dimensionless strain using photon calibrator systems as length fiducials (Viets et al. 2018; Acernese et al. 2018; Bhattacharjee et al. 2021; Estevez et al. 2021). Additionally, the LIGO and Virgo datasets have undergone noise subtraction to remove persistent noise sources measured using witness auxiliary sensors (Davis et al. 2019; Vajente et al. 2020; Estevez et al. 2019; Rolland et al. 2019). Finally, data quality categories based on information of the detectors and investigations of noise sources during the observing run are provided to reduce the number of false alarms (Davis et al. 2021).

Table 1. Analyzed time in days for different instrument observing combinations. We use here the abbreviations H, L, and V for the LIGO-Hanford, LIGO-Livingston, and Virgo observatories respectively. Only the indicated combination of observatories were operating for each time period, hence each is exclusive of all others.

Observation	HLV	HL	HV	LV	H	L	V
O1	-	48.6	-	-	27.6	17.0	-
O2	15.2	103.3	1.7	2.2	37.8	33.0	1.7
O3a	79.7	26.1	17.4	25.2	5.6	6.4	15.7
All	95.0	178.0	19.1	27.4	70.9	56.4	17.4

The time evolution of the BNS range for each observatory and the distribution of detector observing times are shown in Fig. 1 and Table 1, respectively. In total, there have been 464 days of Advanced LIGO and Virgo observing time. Two or more detectors were observing during 320 days, of which 95 days were joint observations of the full LIGO-Hanford, LIGO-Livingston and Virgo network.

The newly released data from O3a adds 176 days of observational data to the existing 288 days from O1 and O2. During the period of O3a, 79.7 days have data from all 3 detectors available, 68.7 days rely on a 2 detector network and 27.7 days contain data only from a single detector. Several upgrades were implemented at the LIGO and Virgo detectors between O2 and O3a to improve the sensitivity of the detectors (Abbott et al. 2020b; Buikema et al. 2020). The maximum BNS range throughout O3a was 142.4 Mpc for LIGO-Livingston, 117.2 Mpc for LIGO-Hanford, and 52.2 Mpc for Virgo.

For the first time, we also include candidates occurring during the 174 days when only one single Advanced LIGO detector was observing. We do not include single-detector candidates from the 17.4 days of Advanced Virgo data.

3. SEARCH FOR COMPACT-BINARY MERGERS

We use matched filtering to extract the signal-to-noise ratio (SNR) of a potential signal (Allen et al. 2012; Brown 2004), as is the standard procedure for the most sensitive gravitational-wave searches where there is an accurate model of the gravitational waveform available (Davies et al. 2020; Messick et al. 2016; Venumadhav et al. 2019b). We assess each potential candidate for consistency with the expected gravitational-wave morphology (Allen 2005; Nitz 2018) and then rank potential candidates (Davies et al. 2020; Mozzon et al. 2020) based on factors including the overall noise rate and each signal's coherence between detectors (Nitz et al. 2017).

The procedure broadly follows the same methods used to construct the prior 2-OGC catalog (Nitz et al. 2019d), but with improvements to the removal of loud transient glitches and more stringent constraints on our suite of signal consistency tests. Detailed configuration files necessary to reproduce the analysis are included in our data release (Nitz & Capano 2021b). In addition, we use a denser bank of templates to reduce loss in sensitivity from mismatch between our template bank and the gravitational-wave signal. The analysis is accomplished using the public and open source PyCBC analysis toolkit (Nitz et al. 2018).

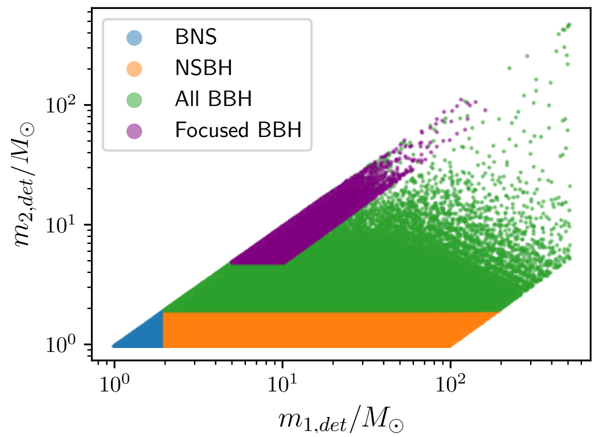

Figure 2. The detector-frame (redshifted) component masses of templates used to search for compact binary mergers. The template bank is constructed in four parts using stochastic placement. The binary neutron star (blue), neutron star–black hole (orange), binary black hole (green), and focused binary black hole (purple) regions are shown. Templates in the focused binary black hole region are colored in purple and bounded by $m_{1,2} > 5\,\mathrm{M}_\odot$, $m_1/m_2 < 2$, and $m_{1,det} + m_{2,det} < 250\,\mathrm{M}_\odot$. The detector-frame masses are related to the source-frame masses through the redshift (z) by $m_{1/2,det} = m_{1/2}(1+z)$, which accounts for the effects of cosmic expansion. This region is responsible for the vast majority of observed BBH mergers, but is composed of only $\sim 3\%$ of the total number of templates (~ 1.3 million), despite placement at higher density than the rest of the search space.

3.1. *Search Space*

To search for gravitational-wave sources using matched filtering, we rely upon accurate models of the gravitational waveform to act as templates. To account for sources with varied component masses and component spins, we construct a discrete bank of templates designed to ensure that for any signal within the target region there is a matching template able to recover its SNR at a prescribed maximum loss. We note that a different criteria would be used to maximize detections at a fixed computational cost (Allen 2021), however, this analysis is not computational limited. As shown in Fig. 2, the search region can be divided into three parts targeting different types of sources, namely, BNS (blue), NSBH (orange), and BBH (green and purple) sources. The template bank is designed to detect non-precessing sources in quasi-circular orbits which can be modelled by two component masses and the spin of each component parallel to the orbital angular momentum. For BNS sources, we allow for matter effects up to $\tilde{\Lambda} < 300$, where $\tilde{\Lambda}$ is a weighted average of the component stars' tidal deformabilities (Flanagan & Hinderer 2008). Inclusion of these effects may become important for future detectors, though have only minor impacts on the sensitivity of current searches (Harry & Lundgren 2021).

The broad BNS, NSBH, and BBH regions are constructed so that signals lose no more than 3% in SNR due to the discreteness of the template bank. The boundaries are similar to those used in our previous catalog (Dal Canton & Harry 2017), however, we no longer restrict each template's duration and instead include templates with component masses up to $500\mathrm{M}_{\odot}$ (detector frame). In addition, there is a separate focused BBH region (shown in purple in Fig. 2) which contains the entirety of known binary black hole sources with the exception of the high mass-ratio merger GW190814 (Abbott et al. 2020e). To ensure the maximum sensitivity to faint signals, we place templates in this region ensuring no more than 0.5% of SNR is lost due to bank discreteness. Stochastic placement (Harry et al. 2009; Ajith et al. 2014) as implemented in the PyCBC toolkit (Nitz et al. 2018) is used to construct each bank.

Despite targeting non-precessing sources, we expect this search retains sensitivity to some types of moderately precessing sources (Abbott et al. 2016), especially if they are short in duration or have orientation near to face-on/off. Searches which neglect precession lose sensitivity to highly precessing sources if the sources are a combination of high mass ratio, highly inclined, and observable for many cycles (Harry et al. 2016). Similarly, we expect this search to lose sensitivity to highly eccentric sources (Ramos-Buades et al. 2020; Wang & Nitz 2021). Separate searches have been conducted focusing on eccentric sources (Nitz & Wang 2021a; Nitz et al. 2019b; Abbott et al. 2019c) and on those sources outside of the regions we consider here (Nitz & Wang 2021b; Abbott et al. 2019a). Where the search methodology or waveform modelling is not yet sufficient, alternate techniques based on looking for coherent excess power are employed on LIGO and Virgo data (Klimenko et al. 2008, 2016; Tiwari et al. 2016).

We employ three waveform models within our search: TaylorF2 (Sathyaprakash & Dhurandhar 1991; Droz et al. 1999; Blanchet 2002; Faye et al. 2012), IMRPhenomD (Khan et al. 2016b), and the reduced order model of SEOBNRv4 (Taracchini et al. 2014; Bohé et al. 2016). TaylorF2 models only the inspiral portion of a gravitational-wave signal and is suitable for cases where the merger would be hidden by the detector noise. As such, it is employed only in the BNS region of our analysis. IMRPhenomD is used within the focused BBH search (purple) and SEOBNRv4 is used everywhere else. Both IMRPhenomD and SEOBNRv4 model the inspiral, merger, and ringdown of a non-precessing binary black hole coalescence. All models include only the dominant gravitational-wave mode. Investigations have been made into incorporating models with higher order modes into gravitational-wave searches (Capano et al. 2013; Harry et al. 2018).

3.2. *Multi-detector Candidates and Significance*

A ranking statistic is assigned to each potential candidate following the procedure in Davies et al. (2020). The statistical significance of any given candidate is assessed by empirically estimating the rate of false alarms at the ranking statistic value associated with a candidate, and is typically reported as an inverse false alarm rate (IFAR). The distribution of false alarms is determined by the creation of numerous analyses which do not contain astrophysical candidates (Babak et al. 2013; Usman et al. 2016). This is achieved by analyzing the data set with time offsets between the detectors large enough to break the time-of-flight requirements for a true astrophysical signal. This procedure has been used successfully in many past analyses (Nitz et al. 2019d,a; Abbott et al. 2019b; Venumadhav et al. 2019b; Abadie et al. 2012; Abbott et al. 2009, 2020b). Note, however, that this method is only applicable when multiple detectors are observing.

The IFAR of the search at the ranking statistic of a given candidate, however, does not answer the question of how likely a given candidate is to be astrophysical in origin, but rather the rate at which the search will produce candidates as statistically significant under the null hypothesis. For candidates which lie in part of the parameter space where a population model can be sufficiently described, as is the case for our focused BBH region, we can predict the rate of astrophysical sources and the distribution of true astrophysical sources which would be observed by our search for a given merger rate. The response of the search to a population of sources is directly measured by adding simulated gravitational-wave signals to the data. We model the full behavior of the search using a two-component mixture model of the expected astrophysical distribution and the empirically measured distribution of false alarms (Farr et al. 2015). A similar procedure has been used in past analyses of gravitational-wave data to assign the probability of astrophysical origin, or $\mathcal{P}_{\mathrm{astro}}$ (Nitz et al. 2019d; Abbott et al. 2020b). For multi-detector candidates which lie outside of the focused BBH region, in regions where the population of candidates is less certain or unknown, we choose not to assign a probability of astrophysical origin.

3.3. *Single-detector Candidates*

In this catalog, we conduct a single-detector analysis of the focused BBH and BNS regions. We rely on the methods introduced in Nitz et al. (2020) to assess the probability of astrophysical origin of observed candidates. We assess the expected signal distribution in the same manner as for multi-detector candidates. However, due to the inability to empirically estimate the noise distribution for occurrences rarer than once per observing period, an extrapolation is needed; Nitz et al. (2020) introduces a purposefully conservative noise model for this purpose. Due to the mismatch in sensitive range between the LIGO and Virgo instruments (factor of 2-3x), we apply the single-detector analysis to time when a single LIGO observatory is operating, irrespective of Virgo's observing status. In order to limit the effects of possible astrophysical contamination, we assess the background using only data collected when both LIGO observatories were observing. This ensures that most strong astrophysical signals can be excised from the data using the multi-detector coincidence analysis first.

4. PARAMETER INFERENCE

We infer the properties of BBH and BNS mergers by performing Bayesian analysis with the help of PyCBC Inference (Biwer et al. 2019). For BBHs, we use the latest version of the IMRPhenomXPHM waveform model (Pratten et al. 2020), which includes subdominant harmonics and effects of precession on a quasi-circular BBH merger. In a recent study, this waveform model was used for doing parameter estimation on events from the first and second observing runs (Mateu-Lucena et al. 2021). We use the dynamical nested sampling algorithm (Higson et al. 2018; Skilling 2006) implemented in the Dynesty software package (Speagle 2020) to sample over the parameter space, which includes chirp mass, mass ratio, spins (radial, polar, and azimuthal), distance, inclination angle, right ascension, declination, coalescence phase, and the merger time. To help with sampler convergence we numerically marginalize over polarization. For each of the events, we use uniform priors on source-frame component masses and merger time. We also assume a distance prior that is uniform in comoving volume; the luminosity distance (D_L) is related to the comoving volume assuming a flat ΛCDM cosmological model (Ade et al. 2015). An isotropic distribution of prior in the sky localization and binary orientation is assumed for each of the events. For the spins, we use uniform priors for the magnitude of the spin and isotropic for the orientation. A low frequency cutoff ($f_{\rm low}$) of 20 Hz is used for the evaluation of the likelihood function for all the detectors and for analyzing all the events except for GW190727_060333 ($f_{\rm low}$ = 50 Hz for LIGO Livingston) and GW190814_211039 ($f_{\rm low}$ = 30 Hz for LIGO Hanford) (Abbott et al. 2020b). In some instances, the raw data contains glitches as described in (Abbott et al. 2020b). Where available, we use the public glitch-subtracted data (for e.g. GW190413_134308, GW190424_180648, GW190425_081805, GW190503_185404, GW190513_205428, GW190514_065416, GW190701_203306, and GW190924_021846) (Vallisneri et al. 2015; Abbott et al. 2021a).

For BNS mergers, we use the IMRPhenomD_NRTidal waveform model (Khan et al. 2016a; Husa et al. 2016; Dietrich et al. 2017, 2019), which includes tidal deformability parameters Λ_1 and Λ_2 of the two component masses. We use similar priors to that of the BBH analyses on component masses, comoving volume, merger time, and orientation. We use a heterodyne method (Cornish 2010; Finstad & Brown 2020; Zackay et al. 2018) to calculate the likelihood function. For the component spins, we assume spins aligned with the orbital angular moment with magnitude $\in [-0.05, 0.05]$. We do not assume a common equation of state for the components; instead, we allow the tidal deformability of the components $\Lambda_{1,2}$ to vary independently of each other, using a prior uniform $\in [0, 5000]$ for both. A low frequency cutoff of 20 Hz is used to estimate the likelihood function.

5. OBSERVATIONAL RESULTS

From the combined analysis of the 2015-2019 public LIGO and Virgo data, we find 55 BBH mergers and 2 BNS mergers. The list of gravitational wave mergers is given in Table 2. For the majority of BBHs we can assess the probability of astrophysical origin. Our catalog includes candidates where $\mathcal{P}_{\rm astro} > 0.5$ or IFAR > 100 years. The marginalized parameter estimates for source-frame component masses, chirp mass, mass ratio, effective spin, luminosity distance, redshift, final mass, and final spin obtained from the posterior distributions are listed in table 4.

Several candidates were independently detected by Virgo, with the Virgo observatory being decisive in the case of two of them. As the gap in sensitivity between the LIGO and Virgo instruments narrows, we expect this to become more commonplace. We identify four candidates in our single-detector analysis of BNS and BBH mergers in LIGO Hanford and LIGO Livingston data as shown in Fig. 3. These are consistent with the previously-reported single-detector analysis of Abbott et al. (2020b).

We find four previously unreported BBH mergers; three, GW190725_174728, GW190916_200658, and GW190926_050336 are near-threshold observations with relatively low SNR. The fourth, GW190925_232845, has SNR ∼ 10 and is found at a false alarm rate

$< 1/100$ years. We find GW190925_232845 has component masses $20.2^{+3.9}_{-2.5}\mathrm{M}_\odot$ and $15.6^{+2.1}_{-2.6}\mathrm{M}_\odot$. While not reported as a new BBH merger detection, this time was noted as part of a recent search for lensed images (McIsaac et al. 2020; Abbott et al. 2021b). The remainder of the multi-detector observed mergers are broadly consistent with previous searches (Venumadhav et al. 2019a; Abbott et al. 2020b, 2019b). Two marginal observations reported in Abbott et al. (2020b), 190426_152155 and 190909_114149, are not assigned high significance in our analysis, but notably, our updated catalog now includes two candidates which were originally reported in Venumadhav et al. (2019a) from O2, GW170202_135657 and GW170403_230611.

Table 2. Gravitational-wave observations from the full search of O1-O3a data with $\mathcal{P}_{\mathrm{astro}} > 0.5$ or IFAR > 100 years. Candidates are sorted by observation time. For each candidate, we show the detectors that were observing at the time, the subset which triggered on the event within our analysis, and the SNR (ρ) reported by the search for each detector. Due to thresholds on the SNR and the ability for the search to select a preferred candidate from many at a given time, there may be no detector SNR associated with a candidate, even if it is observing at the time. For multi-detector candidates, we show the false alarm rate of the entire search at the threshold of its ranking statistic value. For BBHs found by our focused BBH search, we give estimates of the probability of astrophysical origin $\mathcal{P}_{\mathrm{astro}}$. We also show our estimates for single-detector candidates, which we note will necessarily be more uncertain, due to the need to extrapolate the background model. GW190425 is assessed using the same conservative extrapolation of the background as for BBH candidates, however, we expect that the noise distribution may be more well-behaved than assumed here for such a long duration signal. Candidates reported here for the first time are in bold.

	Event	GPS Time	Observing	Triggered	$\mathcal{P}_{\mathrm{astro}}$	IFAR [yr]	ρ_H	ρ_L	ρ_V
1	GW150914_095045	1126259462.43	HL	HL	1.00	> 100	19.9	13.0	-
2	GW151012_095443	1128678900.45	HL	HL	1.00	> 100	6.9	6.6	-
3	GW151226_033853	1135136350.65	HL	HL	1.00	> 100	10.5	7.4	-
4	GW170104_101158	1167559936.60	HL	HL	1.00	> 100	8.9	9.6	-
5	GW170121_212536	1169069154.58	HL	HL	1.00	16	5.2	8.9	-
6	GW170202_135657	1170079035.73	HL	HL	0.81	0.50	5.4	6.2	-
7	GW170304_163753	1172680691.37	HL	HL	0.70	0.25	4.6	7.0	-
8	GW170403_230611	1175295989.23	HL	HL	0.71	0.25	5.2	5.5	-
9	GW170608_020116	1180922494.49	HL	HL	1.00	> 100	12.4	9.0	-
10	GW170727_010430	1185152688.03	HL	HL	1.00	71	4.7	7.5	-
11	GW170729_185629	1185389807.32	HL	HL	0.99	28	7.5	6.9	-
12	GW170809_082821	1186302519.75	HLV	HL	1.00	> 100	6.7	10.7	-
13	GW170814_103043	1186741861.53	HLV	HL	1.00	> 100	9.2	13.7	-
14	GW170817_124104	1187008882.45	HLV	HL	-	> 100	18.3	25.5	-
15	GW170818_022509	1187058327.08	HLV	HL	1.00	5.26	4.5	9.6	-
16	GW170823_131358	1187529256.52	HL	HL	1.00	> 100	6.6	9.1	-
17	GW190408_181802	1238782700.28	HLV	HL	1.00	> 100	9.2	10.3	-
18	GW190412_053044	1239082262.17	HLV	HL	1.00	> 100	8.2	14.9	-
19	GW190413_052954	1239168612.50	HLV	HL	0.99	1.45	5.2	6.7	-
20	GW190413_134308	1239198206.74	HLV	HL	0.99	6.39	5.4	7.8	-
21	GW190421_213856	1239917954.25	HL	HL	1.00	> 100	7.9	6.3	-
22	GW190424_180648	1240164426.14	L	L	0.81	-	-	9.9	-
23	GW190425_081805	1240215503.02	LV	L	0.50	-	-	11.9	-
24	GW190503_185404	1240944862.29	HLV	HL	1.00	> 100	9.1	7.6	-
25	GW190512_180714	1241719652.42	HLV	HL	1.00	> 100	5.9	10.8	-
26	GW190513_205428	1241816086.74	HLV	HLV	1.00	> 100	8.8	7.7	4.0
27	GW190514_065416	1241852074.85	HL	HL	0.85	0.19	6.1	5.3	-
28	GW190517_055101	1242107479.83	HLV	HL	1.00	66	6.8	7.9	-
29	GW190519_153544	1242315362.38	HLV	HL	1.00	> 100	7.8	9.3	-
30	GW190521_030229	1242442967.44	HLV	HL	1.00	> 100	8.4	12.0	-
31	GW190521_074359	1242459857.47	HL	HL	1.00	> 100	12.1	21.0	-
32	GW190527_092055	1242984073.79	HL	HL	0.93	0.37	5.0	7.0	-
33	GW190602_175927	1243533585.10	HLV	HL	1.00	> 100	6.2	10.8	-

Table 2. (Continued) Gravitational-wave observations from the full search of O1-O3a data with $\mathcal{P}_{\rm astro} > 0.5$ or IFAR > 100 years. Candidates are sorted by observation time. For each candidate, we show the detectors that were observing at the time, the subset which triggered on the event within our analysis, and the SNR (ρ) reported by the search for each detector. Due to thresholds on the SNR and the ability for the search to select a preferred candidate from many at a given time, there may be no detector SNR associated with a candidate, even if it is observing at the time. For multi-detector candidates, we show the false alarm rate of the entire search at the threshold of its ranking statistic value. For BBHs found by our focused BBH search, we give estimates of the probability of astrophysical origin $\mathcal{P}_{\rm astro}$. We also show our estimates for single-detector candidates, which we note will necessarily be more uncertain, due to the need to extrapolate the background model. GW190425 is assessed using the same conservative extrapolation of the background as for BBH candidates, however, we expect that the noise distribution may be more well-behaved than assumed here for such a long duration signal. Candidates reported here for the first time are in bold.

	Event	GPS Time	Observing	Triggered	$\mathcal{P}_{\rm astro}$	IFAR [yr]	ρ_H	ρ_L	ρ_V
34	GW190620_030421	1245035079.31	LV	L	0.85	-	-	11.2	-
35	GW190630_185205	1245955943.18	LV	LV	1.00	0.18	-	14.7	4.0
36	GW190701_203306	1246048404.58	HLV	HLV	1.00	0.13	6.0	8.9	5.7
37	GW190706_222641	1246487219.33	HLV	HL	1.00	> 100	9.4	8.6	-
38	GW190707_093326	1246527224.17	HL	HL	1.00	> 100	7.9	9.6	-
39	GW190708_232457	1246663515.38	LV	L	0.85	-	-	12.6	-
40	GW190719_215514	1247608532.92	HL	HL	0.89	0.25	5.6	5.7	-
41	GW190720_000836	1247616534.71	HLV	HL	1.00	> 100	6.8	7.7	-
42	**GW190725_174728**	1248112066.46	HLV	HL	0.91	0.41	5.4	7.3	-
43	GW190727_060333	1248242631.98	HLV	HL	1.00	> 100	7.9	8.1	-
44	GW190728_064510	1248331528.53	HLV	HL	1.00	> 100	7.5	10.6	-
45	GW190731_140936	1248617394.64	HL	HL	0.93	0.43	5.2	6.0	-
46	GW190803_022701	1248834439.88	HLV	HL	0.99	2.40	5.6	6.7	-
47	GW190814_211039	1249852257.01	HLV	HL	-	> 100	11.0	21.1	-
48	GW190828_063405	1251009263.76	HLV	HL	1.00	> 100	10.3	11.2	-
49	GW190828_065509	1251010527.89	HLV	HL	1.00	> 100	7.3	7.4	-
50	GW190910_112807	1252150105.32	LV	L	0.87	-	-	13.4	-
51	GW190915_235702	1252627040.70	HLV	HL	1.00	> 100	9.0	8.6	-
52	**GW190916_200658**	1252699636.90	HLV	HL	0.88	0.22	4.9	5.9	-
53	GW190924_021846	1253326744.84	HLV	HL	1.00	> 100	6.7	10.8	-
54	**GW190925_232845**	1253489343.12	HV	HV	1.00	> 100	8.2	-	5.4
55	**GW190926_050336**	1253509434.07	HLV	HL	0.88	0.27	5.4	5.6	-
56	GW190929_012149	1253755327.50	HLV	HL	0.98	3.08	5.8	7.4	-
57	GW190930_133541	1253885759.24	HL	HL	1.00	> 100	6.7	7.4	-

Table 3. The selection of sub-threshold candidates with $\mathcal{P}_{\rm astro} > 0.2$ or IFAR > 0.5 from the full search of O1-O3a data. Candidates are sorted by the observation time. The complete set of sub-threshold candidate is available in the data release and includes a selection of full parameter estimates. Here we show the detector-frame (redshifted) parameters of the template which triggered on the candidate, along with the reported SNRs (ρ) from each detector.

	Event	GPS Time	Observing	Triggered	$\mathcal{P}_{\rm astro}$	IFAR	ρ_H	ρ_L	ρ_V	$m_{1,\rm det}/\mathrm{M}_\odot$	$m_{2,\rm det}/\mathrm{M}_\odot$	$\chi_{\rm eff}$
1	151011_192749	1128626886.60	HL	HL	0.21	0.02	4.7	6.8	-	33.5	65.6	0.1
2	151205_195525	1133380542.41	HL	HL	0.25	0.03	5.9	4.8	-	81.6	77.7	0.1
3	170425_055334	1177134832.19	HL	HL	0.41	0.07	5.3	5.8	-	46.1	65.0	0.1
4	170704_202003	1183234821.62	HL	HL	0.34	0.05	5.1	6.5	-	10.0	13.2	-0.0
5	170722_065503	1184741721.32	HL	HL	-	0.89	5.0	7.3	-	1.7	1.3	-0.0
6	190404_142514	1238423132.99	HL	HL	0.44	0.02	5.1	5.9	-	22.5	24.5	0.1
7	190426_053949	1240292407.21	HLV	HL	0.32	0.01	5.2	6.1	-	20.7	20.0	0.2
8	190427_180650	1240423628.68	HLV	HL	0.41	0.02	5.8	6.8	-	13.0	7.9	-0.0

Table 3. (Continued) The selection of sub-threshold candidates with $\mathcal{P}_{\rm astro} > 0.2$ or IFAR > 0.5 from the full search of O1-O3a data. Candidates are sorted by the observation time. The complete set of sub-threshold candidate is available in the data release and includes a selection of full parameter estimates. Here we show the detector-frame (redshifted) parameters of the template which triggered on the candidate, along with the reported SNRs (ρ) from each detector.

9	190509_004120	1241397698.79	HLV	HL	0.31	0.01	4.7	6.2	-	30.1	28.2	-0.0
10	190524_134109	1242740487.36	HLV	HL	0.21	0.01	4.3	6.0	-	123.3	77.2	0.2
11	190530_030659	1243220837.97	HLV	HL	0.31	0.01	5.2	5.8	-	26.3	45.4	0.2
12	190630_135302	1245938000.49	HL	HL	0.23	0.01	5.1	5.8	-	32.6	19.2	0.0
13	190704_104834	1246272532.92	HLV	HL	0.26	0.01	7.0	5.5	-	5.0	5.4	0.1
14	190707_071722	1246519060.10	HLV	HL	0.21	0.01	6.0	5.7	-	10.7	14.1	0.0
15	190805_105432	1249037690.78	HL	HL	0.41	0.02	4.8	6.5	-	9.4	18.3	-0.1
16	190808_230535	1249340753.59	HLV	HL	0.31	0.01	5.0	6.5	-	13.6	13.6	0.2
17	190821_050019	1250398837.88	HLV	HL	0.23	0.01	5.2	5.6	-	26.8	17.0	-0.1

Table 4. Bayesian parameter estimation for the 57 detections in the entire O1-O3a data. We report the median value and 90% credible interval for the source-frame component mass m_1 and m_2, chirp mass $\mathcal{M}$, mass ratio q, effective spin $\chi_{\rm eff}$, luminosity distance $D_{\rm L}$, redshift z, and remnant mass and spin M_f and χ_f, respectively. The signal-to-noise ratio (SNR) is computed from the maximum likelihood with polarization angle being numerically marginalized for BBH events and with phase analytically marginalized for BNS events. Candidates reported here for the first time are in bold.

	Event	$m_1/M_\odot$	$m_2/M_\odot$	$\mathcal{M}/M_\odot$	q	$\chi_{\rm eff}$	$D_{\rm L}$/Mpc	z	$M_{\rm f}/M_\odot$	χ_f	SNR
1	GW150914_095045	$34.7^{+4.7}_{-2.8}$	$29.8^{+2.8}_{-4.4}$	$27.9^{+1.4}_{-1.3}$	$1.2^{+0.4}_{-0.1}$	$-0.03^{+0.11}_{-0.13}$	534^{+123}_{-157}	$0.11^{+0.02}_{-0.03}$	$61.5^{+2.9}_{-2.7}$	$0.67^{+0.03}_{-0.05}$	23.8
2	GW151012_095443	$27.0^{+10.5}_{-7.9}$	$11.8^{+4.3}_{-3.1}$	$15.2^{+1.1}_{-0.9}$	$2.3^{+2.0}_{-1.1}$	$0.05^{+0.22}_{-0.15}$	927^{+456}_{-329}	$0.18^{+0.08}_{-0.06}$	$37.4^{+7.7}_{-4.8}$	$0.62^{+0.08}_{-0.08}$	9.8
3	GW151226_033853	$13.8^{+11.5}_{-3.2}$	$7.5^{+2.2}_{-2.7}$	$8.8^{+0.3}_{-0.2}$	$1.8^{+3.4}_{-0.7}$	$0.2^{+0.23}_{-0.07}$	489^{+139}_{-196}	$0.1^{+0.03}_{-0.04}$	$20.3^{+9.1}_{-1.3}$	$0.72^{+0.02}_{-0.04}$	13.3
4	GW170104_101158	$29.1^{+6.3}_{-4.4}$	$20.5^{+4.2}_{-4.3}$	$21.0^{+1.9}_{-1.5}$	$1.4^{+0.7}_{-0.4}$	$-0.06^{+0.15}_{-0.18}$	1077^{+384}_{-458}	$0.21^{+0.07}_{-0.08}$	$47.5^{+4.2}_{-3.3}$	$0.65^{+0.06}_{-0.09}$	13.7
5	GW170121_212536	$33.0^{+8.7}_{-5.6}$	$25.1^{+5.6}_{-6.4}$	$24.9^{+3.7}_{-3.2}$	$1.3^{+0.8}_{-0.3}$	$-0.19^{+0.23}_{-0.29}$	1164^{+981}_{-673}	$0.23^{+0.16}_{-0.12}$	$55.9^{+7.9}_{-7.0}$	$0.61^{+0.08}_{-0.13}$	10.9
6	GW170202_135657	$30.9^{+12.6}_{-8.2}$	$13.7^{+6.3}_{-3.8}$	$17.5^{+3.1}_{-1.5}$	$2.3^{+2.1}_{-1.1}$	$-0.08^{+0.29}_{-0.31}$	1422^{+735}_{-608}	$0.27^{+0.12}_{-0.11}$	$43.6^{+9.7}_{-5.6}$	$0.54^{+0.17}_{-0.15}$	8.5
7	GW170304_163753	$44.5^{+14.7}_{-9.0}$	$31.7^{+9.3}_{-11.2}$	$32.1^{+6.8}_{-5.5}$	$1.4^{+1.3}_{-0.3}$	$0.1^{+0.27}_{-0.26}$	2354^{+1584}_{-1293}	$0.42^{+0.22}_{-0.21}$	$72.4^{+15.0}_{-10.8}$	$0.7^{+0.09}_{-0.13}$	8.7
8	GW170403_230611	$49.1^{+16.4}_{-10.5}$	$35.8^{+11.4}_{-12.4}$	$35.9^{+8.7}_{-6.7}$	$1.3^{+1.1}_{-0.3}$	$-0.21^{+0.33}_{-0.35}$	2967^{+2204}_{-1540}	$0.51^{+0.29}_{-0.24}$	$81.4^{+19.0}_{-14.0}$	$0.6^{+0.11}_{-0.17}$	7.7
9	GW170608_020116	$10.6^{+3.1}_{-1.3}$	$8.0^{+1.1}_{-1.7}$	$8.0^{+0.2}_{-0.2}$	$1.3^{+0.9}_{-0.3}$	$0.07^{+0.11}_{-0.06}$	321^{+129}_{-110}	$0.07^{+0.03}_{-0.02}$	$17.8^{+1.5}_{-0.6}$	$0.69^{+0.02}_{-0.03}$	15.2
10	GW170727_010430	$41.3^{+12.1}_{-7.6}$	$30.8^{+8.0}_{-8.9}$	$30.7^{+5.5}_{-4.6}$	$1.3^{+0.9}_{-0.3}$	$-0.04^{+0.23}_{-0.3}$	2153^{+1529}_{-1050}	$0.39^{+0.22}_{-0.17}$	$69.1^{+11.9}_{-9.7}$	$0.66^{+0.08}_{-0.14}$	8.8
11	GW170729_185629	$53.8^{+12.1}_{-11.8}$	$31.6^{+13.0}_{-10.4}$	$35.1^{+7.9}_{-5.8}$	$1.7^{+1.1}_{-0.6}$	$0.28^{+0.22}_{-0.29}$	2236^{+1590}_{-1215}	$0.4^{+0.23}_{-0.2}$	$80.9^{+15.0}_{-11.0}$	$0.76^{+0.08}_{-0.18}$	10.8
12	GW170809_082821	$33.9^{+8.2}_{-5.0}$	$24.5^{+4.7}_{-5.5}$	$24.9^{+2.1}_{-1.6}$	$1.4^{+0.8}_{-0.3}$	$0.08^{+0.16}_{-0.16}$	1069^{+293}_{-364}	$0.21^{+0.05}_{-0.07}$	$55.8^{+4.8}_{-3.5}$	$0.69^{+0.06}_{-0.08}$	12.4
13	GW170814_103043	$30.9^{+5.4}_{-3.2}$	$24.9^{+2.9}_{-4.0}$	$24.0^{+1.3}_{-1.0}$	$1.2^{+0.5}_{-0.2}$	$0.07^{+0.12}_{-0.12}$	593^{+149}_{-207}	$0.12^{+0.03}_{-0.04}$	$53.2^{+3.0}_{-2.3}$	$0.7^{+0.04}_{-0.04}$	17.4
14	GW170817_124104	$1.4^{+0.1}_{-0.1}$	$1.3^{+0.1}_{-0.1}$	$1.2^{+0.0}_{-0.0}$	$1.1^{+0.2}_{-0.1}$	$-0.0^{+0.01}_{-0.01}$	43^{+5}_{-10}	$0.01^{+0.0}_{-0.0}$	-	-	32.7
15	GW170818_022509	$35.2^{+7.1}_{-4.6}$	$27.0^{+4.4}_{-5.3}$	$26.7^{+2.2}_{-1.9}$	$1.3^{+0.6}_{-0.3}$	$-0.07^{+0.19}_{-0.23}$	1073^{+434}_{-411}	$0.21^{+0.07}_{-0.07}$	$59.6^{+4.7}_{-4.0}$	$0.65^{+0.07}_{-0.09}$	11.8
16	GW170823_131358	$38.1^{+9.7}_{-6.0}$	$28.6^{+6.4}_{-7.5}$	$28.4^{+4.2}_{-3.1}$	$1.3^{+0.8}_{-0.3}$	$0.05^{+0.2}_{-0.23}$	1965^{+810}_{-873}	$0.36^{+0.12}_{-0.14}$	$63.5^{+9.0}_{-6.3}$	$0.69^{+0.07}_{-0.11}$	11.4
17	GW190408_181802	$24.6^{+5.2}_{-3.4}$	$18.4^{+3.4}_{-3.7}$	$18.3^{+1.8}_{-1.2}$	$1.3^{+0.6}_{-0.3}$	$-0.04^{+0.13}_{-0.16}$	1585^{+447}_{-625}	$0.3^{+0.07}_{-0.11}$	$41.1^{+3.9}_{-2.7}$	$0.66^{+0.05}_{-0.07}$	14.0
18	GW190412_053044	$30.4^{+5.8}_{-4.2}$	$8.2^{+1.2}_{-1.1}$	$13.2^{+0.5}_{-0.3}$	$3.7^{+1.4}_{-0.9}$	$0.25^{+0.12}_{-0.1}$	757^{+156}_{-200}	$0.15^{+0.03}_{-0.04}$	$37.5^{+4.9}_{-3.2}$	$0.65^{+0.04}_{-0.03}$	19.1
19	GW190413_052954	$34.7^{+11.2}_{-6.7}$	$25.1^{+6.7}_{-7.3}$	$25.4^{+4.8}_{-3.7}$	$1.4^{+1.0}_{-0.3}$	$-0.02^{+0.27}_{-0.33}$	3193^{+1784}_{-1366}	$0.54^{+0.24}_{-0.2}$	$57.3^{+10.7}_{-7.9}$	$0.66^{+0.09}_{-0.15}$	9.0
20	GW190413_134308	$51.6^{+16.9}_{-12.7}$	$31.2^{+11.4}_{-11.9}$	$34.1^{+7.5}_{-6.4}$	$1.6^{+1.6}_{-0.6}$	$-0.01^{+0.27}_{-0.35}$	3835^{+2665}_{-1899}	$0.63^{+0.34}_{-0.27}$	$79.4^{+16.0}_{-12.9}$	$0.64^{+0.11}_{-0.25}$	9.9
21	GW190421_213856	$42.2^{+10.8}_{-7.8}$	$31.4^{+8.5}_{-10.6}$	$31.1^{+6.0}_{-5.1}$	$1.3^{+1.1}_{-0.3}$	$-0.06^{+0.23}_{-0.3}$	2679^{+1605}_{-1251}	$0.47^{+0.22}_{-0.19}$	$70.1^{+12.3}_{-9.8}$	$0.65^{+0.08}_{-0.15}$	9.9
22	GW190424_180648	$40.2^{+10.9}_{-7.1}$	$30.7^{+7.3}_{-8.4}$	$30.3^{+5.1}_{-4.4}$	$1.3^{+0.8}_{-0.3}$	$0.09^{+0.22}_{-0.27}$	2134^{+1466}_{-1115}	$0.38^{+0.21}_{-0.18}$	$67.6^{+10.9}_{-9.3}$	$0.7^{+0.07}_{-0.12}$	10.3
23	GW190425_081805	$1.8^{+0.2}_{-0.1}$	$1.5^{+0.1}_{-0.1}$	$1.4^{+0.0}_{-0.0}$	$1.2^{+0.3}_{-0.2}$	$0.02^{+0.02}_{-0.02}$	174^{+46}_{-43}	$0.04^{+0.01}_{-0.01}$	-	-	12.4
24	GW190503_185404	$42.5^{+10.9}_{-8.5}$	$27.5^{+8.1}_{-8.7}$	$29.2^{+4.8}_{-3.9}$	$1.5^{+1.2}_{-0.5}$	$-0.04^{+0.22}_{-0.29}$	1478^{+608}_{-619}	$0.28^{+0.1}_{-0.11}$	$66.9^{+10.0}_{-7.3}$	$0.64^{+0.09}_{-0.18}$	12.2
25	GW190512_180714	$23.2^{+6.1}_{-5.8}$	$12.5^{+3.6}_{-2.7}$	$14.6^{+1.4}_{-0.9}$	$1.9^{+1.1}_{-0.8}$	$0.04^{+0.14}_{-0.15}$	1499^{+481}_{-618}	$0.28^{+0.08}_{-0.11}$	$34.4^{+4.3}_{-3.5}$	$0.65^{+0.06}_{-0.07}$	12.0
26	GW190513_205428	$35.2^{+10.7}_{-9.3}$	$18.1^{+7.4}_{-5.0}$	$21.5^{+3.4}_{-2.2}$	$1.9^{+1.4}_{-0.9}$	$0.14^{+0.23}_{-0.21}$	2195^{+833}_{-815}	$0.39^{+0.12}_{-0.13}$	$51.4^{+8.1}_{-6.4}$	$0.69^{+0.1}_{-0.13}$	12.0
27	GW190514_065416	$41.4^{+18.8}_{-9.6}$	$28.9^{+9.6}_{-9.7}$	$29.8^{+7.6}_{-5.7}$	$1.4^{+1.3}_{-0.4}$	$-0.17^{+0.3}_{-0.35}$	3704^{+2662}_{-1939}	$0.61^{+0.34}_{-0.28}$	$67.8^{+18.5}_{-12.5}$	$0.6^{+0.11}_{-0.18}$	8.1
28	GW190517_055101	$38.8^{+10.5}_{-8.2}$	$24.4^{+6.4}_{-5.8}$	$26.6^{+3.2}_{-3.6}$	$1.6^{+0.9}_{-0.5}$	$0.52^{+0.16}_{-0.19}$	1839^{+1438}_{-847}	$0.34^{+0.21}_{-0.14}$	$59.6^{+8.1}_{-8.2}$	$0.85^{+0.04}_{-0.07}$	11.4
29	GW190519_153544	$63.7^{+10.7}_{-11.2}$	$39.7^{+12.4}_{-13.6}$	$43.0^{+7.0}_{-7.6}$	$1.6^{+1.1}_{-0.5}$	$0.32^{+0.2}_{-0.25}$	2669^{+1877}_{-1021}	$0.46^{+0.26}_{-0.16}$	$97.7^{+12.8}_{-12.4}$	$0.76^{+0.08}_{-0.12}$	13.6

Table 4. (Continued) Bayesian parameter estimation for the 57 detections in the entire O1-O3a data. We report the median value and 90% credible interval for the source-frame component mass m_1 and m_2, chirp mass $\mathcal{M}$, mass ratio q, effective spin $\chi_{\rm eff}$, luminosity distance $D_{\rm L}$, redshift z, and remnant mass and spin M_f and χ_f, respectively. The signal-to-noise ratio (SNR) is computed from the maximum likelihood with polarization angle being numerically marginalized for BBH events and with phase analytically marginalized for BNS events. Candidates reported here for the first time are in bold.

	Event	$m_1/M_\odot$	$m_2/M_\odot$	$\mathcal{M}/M_\odot$	q	$\chi_{\rm eff}$	$D_{\rm L}$/Mpc	z	$M_{\rm f}/M_\odot$	χ_f	SNR
30	GW190521_030229	$101.7^{+27.6}_{-21.4}$	$57.6^{+19.6}_{-28.7}$	$64.9^{+12.1}_{-14.2}$	$1.8^{+2.8}_{-0.6}$	$-0.21^{+0.48}_{-0.4}$	2833^{+2705}_{-1412}	$0.49^{+0.36}_{-0.22}$	$152.0^{+25.5}_{-17.0}$	$0.54^{+0.21}_{-0.47}$	15.2
31	GW190521_074359	$42.7^{+4.4}_{-4.0}$	$33.2^{+5.9}_{-5.3}$	$32.6^{+2.8}_{-2.4}$	$1.3^{+0.3}_{-0.2}$	$0.09^{+0.1}_{-0.11}$	1112^{+410}_{-434}	$0.22^{+0.07}_{-0.08}$	$72.1^{+5.4}_{-4.4}$	$0.7^{+0.04}_{-0.04}$	24.4
32	GW190527_092055	$37.5^{+19.7}_{-9.1}$	$20.9^{+9.3}_{-8.7}$	$23.6^{+6.7}_{-3.7}$	$1.8^{+2.6}_{-0.7}$	$0.09^{+0.23}_{-0.27}$	2340^{+1903}_{-1119}	$0.42^{+0.27}_{-0.18}$	$56.3^{+17.2}_{-8.6}$	$0.67^{+0.1}_{-0.24}$	8.7
33	GW190602_175927	$70.6^{+16.9}_{-13.4}$	$43.6^{+14.4}_{-17.3}$	$47.3^{+8.4}_{-8.7}$	$1.6^{+1.6}_{-0.5}$	$0.12^{+0.24}_{-0.27}$	2897^{+1713}_{-1145}	$0.5^{+0.23}_{-0.17}$	$108.8^{+15.7}_{-13.8}$	$0.69^{+0.1}_{-0.16}$	12.2
34	GW190620_030421	$62.8^{+19.3}_{-15.2}$	$28.5^{+13.8}_{-13.8}$	$35.9^{+7.0}_{-9.9}$	$2.2^{+2.7}_{-1.0}$	$0.27^{+0.22}_{-0.68}$	2800^{+1567}_{-1564}	$0.48^{+0.21}_{-0.24}$	$86.8^{+16.9}_{-10.7}$	$0.73^{+0.1}_{-0.58}$	12.1
35	GW190630_185205	$33.7^{+6.5}_{-5.2}$	$23.0^{+5.1}_{-4.7}$	$24.0^{+2.3}_{-1.5}$	$1.5^{+0.7}_{-0.4}$	$0.12^{+0.14}_{-0.15}$	1192^{+498}_{-409}	$0.23^{+0.08}_{-0.07}$	$54.3^{+4.2}_{-3.9}$	$0.7^{+0.05}_{-0.09}$	15.3
36	GW190701_203306	$55.2^{+10.6}_{-7.4}$	$41.2^{+8.4}_{-11.4}$	$41.0^{+5.0}_{-4.8}$	$1.3^{+0.8}_{-0.3}$	$-0.09^{+0.22}_{-0.28}$	2015^{+691}_{-671}	$0.37^{+0.1}_{-0.11}$	$91.9^{+10.0}_{-8.4}$	$0.64^{+0.08}_{-0.13}$	11.8
37	GW190706_222641	$70.2^{+13.6}_{-15.2}$	$37.0^{+13.7}_{-13.1}$	$43.0^{+9.1}_{-7.2}$	$1.9^{+1.4}_{-0.7}$	$0.19^{+0.28}_{-0.35}$	4111^{+2188}_{-1730}	$0.66^{+0.28}_{-0.24}$	$101.4^{+16.3}_{-12.5}$	$0.71^{+0.11}_{-0.22}$	12.6
38	GW190707_093326	$12.2^{+2.4}_{-2.3}$	$7.8^{+1.4}_{-1.3}$	$8.4^{+0.4}_{-0.3}$	$1.6^{+0.7}_{-0.5}$	$-0.04^{+0.1}_{-0.09}$	901^{+278}_{-332}	$0.18^{+0.05}_{-0.06}$	$19.1^{+1.4}_{-1.2}$	$0.64^{+0.03}_{-0.03}$	12.8
39	GW190708_232457	$17.8^{+4.5}_{-2.4}$	$13.0^{+2.0}_{-2.9}$	$13.2^{+0.7}_{-0.7}$	$1.4^{+0.8}_{-0.3}$	$0.01^{+0.12}_{-0.09}$	873^{+322}_{-329}	$0.18^{+0.06}_{-0.06}$	$29.5^{+2.4}_{-1.6}$	$0.67^{+0.03}_{-0.05}$	12.7
40	GW190719_215514	$38.0^{+41.5}_{-11.1}$	$20.7^{+13.8}_{-8.2}$	$23.6^{+17.1}_{-4.5}$	$1.8^{+2.7}_{-0.8}$	$0.22^{+0.36}_{-0.3}$	3607^{+3356}_{-1776}	$0.6^{+0.42}_{-0.26}$	$55.9^{+46.0}_{-10.6}$	$0.72^{+0.13}_{-0.2}$	7.9
41	GW190720_000836	$12.9^{+6.4}_{-2.8}$	$7.7^{+1.9}_{-2.4}$	$8.6^{+0.6}_{-0.5}$	$1.7^{+1.9}_{-0.6}$	$0.18^{+0.17}_{-0.1}$	1055^{+475}_{-413}	$0.21^{+0.08}_{-0.08}$	$19.8^{+4.2}_{-1.9}$	$0.71^{+0.03}_{-0.04}$	10.7
42	**GW190725_174728**	$10.7^{+16.1}_{-1.5}$	$7.0^{+1.8}_{-3.6}$	$7.7^{+0.4}_{-0.7}$	$1.5^{+6.3}_{-0.4}$	$-0.07^{+0.44}_{-0.09}$	802^{+688}_{-323}	$0.16^{+0.12}_{-0.06}$	$17.8^{+12.0}_{-1.8}$	$0.63^{+0.05}_{-0.06}$	8.6
43	GW190727_060333	$38.4^{+8.5}_{-5.6}$	$29.1^{+6.3}_{-8.3}$	$28.7^{+4.4}_{-3.4}$	$1.3^{+0.8}_{-0.3}$	$0.05^{+0.22}_{-0.24}$	3102^{+1236}_{-1132}	$0.53^{+0.17}_{-0.17}$	$64.0^{+9.0}_{-6.4}$	$0.69^{+0.08}_{-0.11}$	11.4
44	GW190728_064510	$12.2^{+6.2}_{-2.2}$	$7.8^{+1.6}_{-2.2}$	$8.5^{+0.5}_{-0.3}$	$1.6^{+1.7}_{-0.5}$	$0.13^{+0.2}_{-0.08}$	1000^{+255}_{-368}	$0.2^{+0.04}_{-0.07}$	$19.2^{+4.2}_{-1.1}$	$0.7^{+0.02}_{-0.04}$	12.7
45	GW190731_140936	$40.9^{+11.9}_{-8.7}$	$29.4^{+9.6}_{-10.8}$	$29.5^{+7.1}_{-5.8}$	$1.4^{+1.2}_{-0.3}$	$0.02^{+0.26}_{-0.29}$	3345^{+2523}_{-1726}	$0.56^{+0.33}_{-0.26}$	$66.7^{+14.4}_{-11.2}$	$0.68^{+0.09}_{-0.16}$	8.1
46	GW190803_022701	$37.6^{+11.1}_{-7.2}$	$27.5^{+7.8}_{-8.6}$	$27.5^{+5.7}_{-4.2}$	$1.3^{+1.0}_{-0.3}$	$-0.0^{+0.24}_{-0.29}$	3289^{+1882}_{-1574}	$0.55^{+0.25}_{-0.23}$	$62.0^{+12.1}_{-8.7}$	$0.67^{+0.08}_{-0.15}$	8.5
47	GW190814_211039	$23.1^{+1.6}_{-2.4}$	$2.6^{+0.2}_{-0.1}$	$6.1^{+0.1}_{-0.1}$	$8.9^{+1.1}_{-1.5}$	$-0.01^{+0.07}_{-0.13}$	241^{+37}_{-37}	$0.05^{+0.01}_{-0.01}$	$25.4^{+1.5}_{-2.2}$	$0.27^{+0.03}_{-0.06}$	25.1
48	GW190828_063405	$31.8^{+5.2}_{-3.9}$	$26.6^{+4.9}_{-5.0}$	$25.0^{+3.7}_{-2.1}$	$1.2^{+0.4}_{-0.2}$	$0.18^{+0.15}_{-0.16}$	2120^{+719}_{-925}	$0.38^{+0.11}_{-0.15}$	$54.9^{+7.6}_{-4.4}$	$0.74^{+0.05}_{-0.06}$	15.8
49	GW190828_065509	$23.5^{+6.0}_{-6.0}$	$10.9^{+3.4}_{-2.2}$	$13.7^{+1.3}_{-1.0}$	$2.2^{+1.1}_{-0.9}$	$0.05^{+0.15}_{-0.16}$	1393^{+657}_{-573}	$0.27^{+0.11}_{-0.1}$	$33.2^{+4.6}_{-4.0}$	$0.63^{+0.06}_{-0.08}$	11.1
50	GW190910_112807	$43.5^{+7.7}_{-7.0}$	$33.5^{+6.4}_{-7.2}$	$33.0^{+3.9}_{-3.9}$	$1.3^{+0.5}_{-0.3}$	$-0.02^{+0.17}_{-0.19}$	1609^{+1139}_{-694}	$0.3^{+0.17}_{-0.12}$	$73.5^{+8.1}_{-8.3}$	$0.67^{+0.06}_{-0.08}$	13.5
51	GW190915_235702	$31.6^{+6.3}_{-4.2}$	$25.0^{+4.3}_{-4.6}$	$24.2^{+2.8}_{-1.9}$	$1.2^{+0.5}_{-0.2}$	$-0.03^{+0.17}_{-0.21}$	1778^{+642}_{-693}	$0.33^{+0.1}_{-0.12}$	$54.0^{+5.8}_{-4.2}$	$0.66^{+0.06}_{-0.08}$	13.2
52	**GW190916_200658**	$45.7^{+17.0}_{-12.3}$	$24.0^{+13.2}_{-10.4}$	$28.0^{+9.0}_{-6.4}$	$1.8^{+2.2}_{-0.8}$	$0.15^{+0.33}_{-0.3}$	4895^{+2814}_{-2333}	$0.77^{+0.34}_{-0.32}$	$67.4^{+17.2}_{-13.5}$	$0.69^{+0.14}_{-0.22}$	7.5
53	GW190924_021846	$9.1^{+2.6}_{-2.2}$	$4.8^{+1.5}_{-0.9}$	$5.7^{+0.2}_{-0.1}$	$1.9^{+1.1}_{-0.8}$	$0.05^{+0.16}_{-0.1}$	637^{+156}_{-192}	$0.13^{+0.03}_{-0.04}$	$13.3^{+1.8}_{-0.9}$	$0.65^{+0.03}_{-0.05}$	11.8
54	**GW190925_232845**	$20.2^{+3.9}_{-2.5}$	$15.6^{+2.1}_{-2.6}$	$15.4^{+1.0}_{-1.0}$	$1.3^{+0.5}_{-0.3}$	$0.05^{+0.13}_{-0.12}$	961^{+423}_{-319}	$0.19^{+0.07}_{-0.06}$	$34.2^{+2.5}_{-2.2}$	$0.69^{+0.05}_{-0.05}$	9.6
55	**GW190926_050336**	$40.1^{+19.1}_{-10.4}$	$23.4^{+10.8}_{-9.2}$	$25.9^{+9.3}_{-5.5}$	$1.7^{+1.7}_{-0.6}$	$-0.04^{+0.26}_{-0.35}$	3634^{+3172}_{-1869}	$0.6^{+0.4}_{-0.27}$	$60.9^{+22.9}_{-11.7}$	$0.63^{+0.11}_{-0.22}$	8.5
56	GW190929_012149	$65.5^{+14.4}_{-16.2}$	$26.4^{+15.8}_{-10.0}$	$35.1^{+9.6}_{-7.1}$	$2.5^{+2.1}_{-1.2}$	$-0.03^{+0.23}_{-0.27}$	3114^{+2486}_{-1366}	$0.53^{+0.33}_{-0.2}$	$89.4^{+16.6}_{-14.3}$	$0.57^{+0.15}_{-0.25}$	9.9
57	GW190930_133541	$11.9^{+5.5}_{-2.0}$	$8.1^{+1.6}_{-2.3}$	$8.5^{+0.5}_{-0.4}$	$1.5^{+1.5}_{-0.4}$	$0.14^{+0.19}_{-0.13}$	772^{+334}_{-317}	$0.16^{+0.06}_{-0.06}$	$19.2^{+3.3}_{-1.3}$	$0.71^{+0.04}_{-0.05}$	9.9

5.1. *Binary Black Holes*

The mass and spin distributions of the observed population of gravitational-wave mergers, along with their localization posteriors, can be used to constrain various formation channels or population synthesis models (O'Shaughnessy et al. 2008; Stevenson et al. 2015; Zevin et al. 2021) and to estimate the rate of mergers (Roulet et al. 2020; Abbott et al. 2020f). In Fig. 4 we show the one-dimensional marginal posteriors on the component masses, effective spin, and luminosity distance for our observed BBH population. Fig. 5 shows the combined posterior for all our observed BBH sources, with and without accounting for the zeroth order selection effect introduced by the variation of signal loudness as a function of intrinsic source parameters.

5.1.1. *GW190521*

GW190521_030229 (GW190521) is the most massive confident detection in our catalog. Initial parameter estimates produced by the LIGO and Virgo Collaborations indicated that its component masses were $85^{+21}_{-14}\rm M_\odot$ and $66^{+17}_{-18}\rm M_\odot$ (Abbott et al. 2020c,d). This would put at least one of the objects in the "upper mass gap" caused by pair-instability supernovae (PISN) (Woosley 2017; Marchant et al. 2019; Stevenson et al. 2019; van Son et al. 2020), suggesting that the event may have been created by a hierarchical merger (Kimball et al. 2020; Liu & Lai 2021; Fragione et al. 2020). This interpretation was challenged in (Nitz & Capano 2021a) which found multiple modes in the mass posterior. The additional modes were at larger mass ratio (extending to

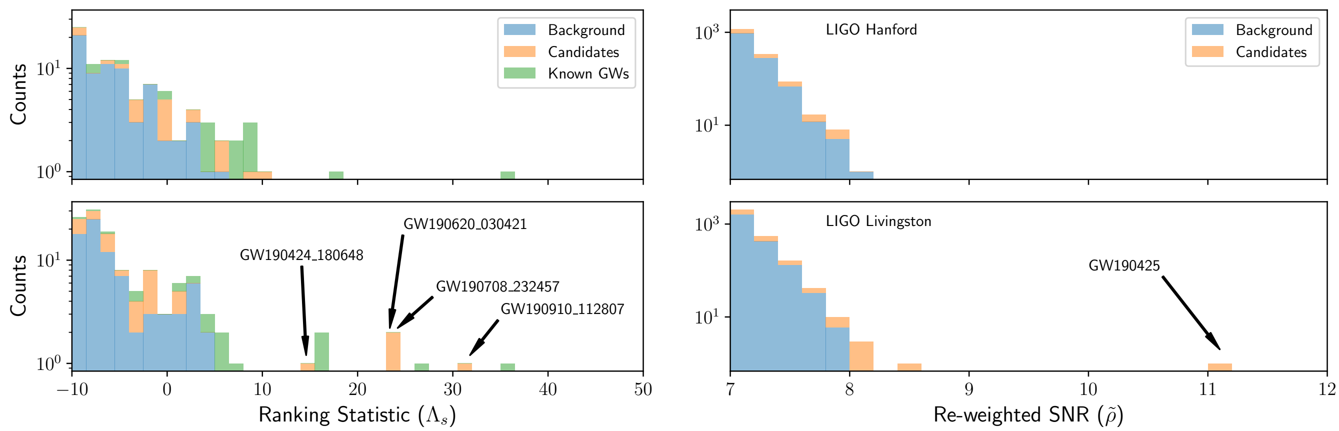

Figure 3. The stacked distributions of single-detector triggered candidates observed when a single LIGO observatory was operating (green), our selected background (blue), and for comparison the distribution of gravitational-wave mergers observed by the multi-detector analysis (orange) as a function of the ranking statistic. To estimate the significance of the candidates, the method of Nitz et al. (2020) is used to extrapolate the background distribution, which allows us to estimate the probability of astrophysical origin. Shown are the results for the BBH (left) and BNS (right) analyses of the LIGO Hanford (top) and LIGO Livingston (bottom) data during O3a.

$q \sim 6$ or $q \sim 10$, depending on the waveform model used), such that component masses straddled the PISN mass gap. However, the highest mass ratio mode (at $q \sim 10$) was found by an earlier version of the IMRPhenomXPHM model. An updated version of the IMRPhenomXPHM model (as used in this work) better accounts for the possibility that the total angular momentum could flip direction, inducing transitional precession. With the corrected version of IMRPhenomXPHM, we no longer find significant support for the mass ratio $q \sim 10$, however support for the mode at $q \sim 6$ remains. This is consistent with the findings of (Estellés et al. 2021).

An analysis using ringdown quasi-normal modes performed in Capano et al. (2021) has shown the more equal-mass scenario, however, may be unlikely. The analysis found strong observational evidence for the presence of the $(lmn) = (330)$ sub-dominant harmonic. This was used to perform a no-hair theorem test, the first instance of black hole spectroscopy using fundamental modes. That a non-zero amplitude was detected for the (330) quasi-normal mode ruled out the possibility that GW190521 was an equal mass binary.

An electromagnetic counterpart was detected by the Zwicky Transient Factory that may be from the same source as GW190521 (Graham et al. 2020). If so, this would suggest that GW190521 occurred in the accretion disk of an active galactic nuclei. Nitz & Capano (2021a) found only marginal support for the event to be in coincidence with the electromagnetic signal, with a log Bayes factor of -4 – 2.3. Using the updated version of IMRPhenomXPHM gives a log Bayes factor of -3.8 – 2.5.

5.1.2. *Other multi-modal events*

In addition to GW190521, we find two other events that show a multimodal distribution in the mass posterior, GW151226_033853 (GW151226) and GW190620_030421. Like GW190521, the secondary peak is at more asymmetric masses, with the maximum likelihood point at $m_2/m_1 \sim 0.2$ for all three events. A large uncertainty in the mass ratio of GW151226 was found by (Mateu-Lucena et al. 2021) using the same waveform model. More recently, a bimodal distribution in the masses of GW151226 was reported by (Chia et al. 2021), again using the same waveform model. However, (Chia et al. 2021) found larger support at more asymmetric masses than we do, as well as a secondary peak in chirp mass that we do not find. Determining whether these events are truly larger mass ratio than previously expected, or if these secondary modes are due to systematic errors in waveform modelling, will require more study.

5.1.3. *High Mass Ratio Mergers*

The events with the largest (unambiguous) mass ratio are GW190814_211039 (GW190814) and GW190412_053044 (GW190412), with a mass ratio of $m_1/m_2 = 8.9^{+1.1}_{-1.5}$ and $3.7^{+1.4}_{-0.9}$, respectively. These estimates are consistent with those found by the LIGO and Virgo Collaborations (Abbott et al. 2020g,e). The smaller object in GW190814 had a mass of $2.6^{+0.2}_{-0.1}\,\mathrm{M}_\odot$,

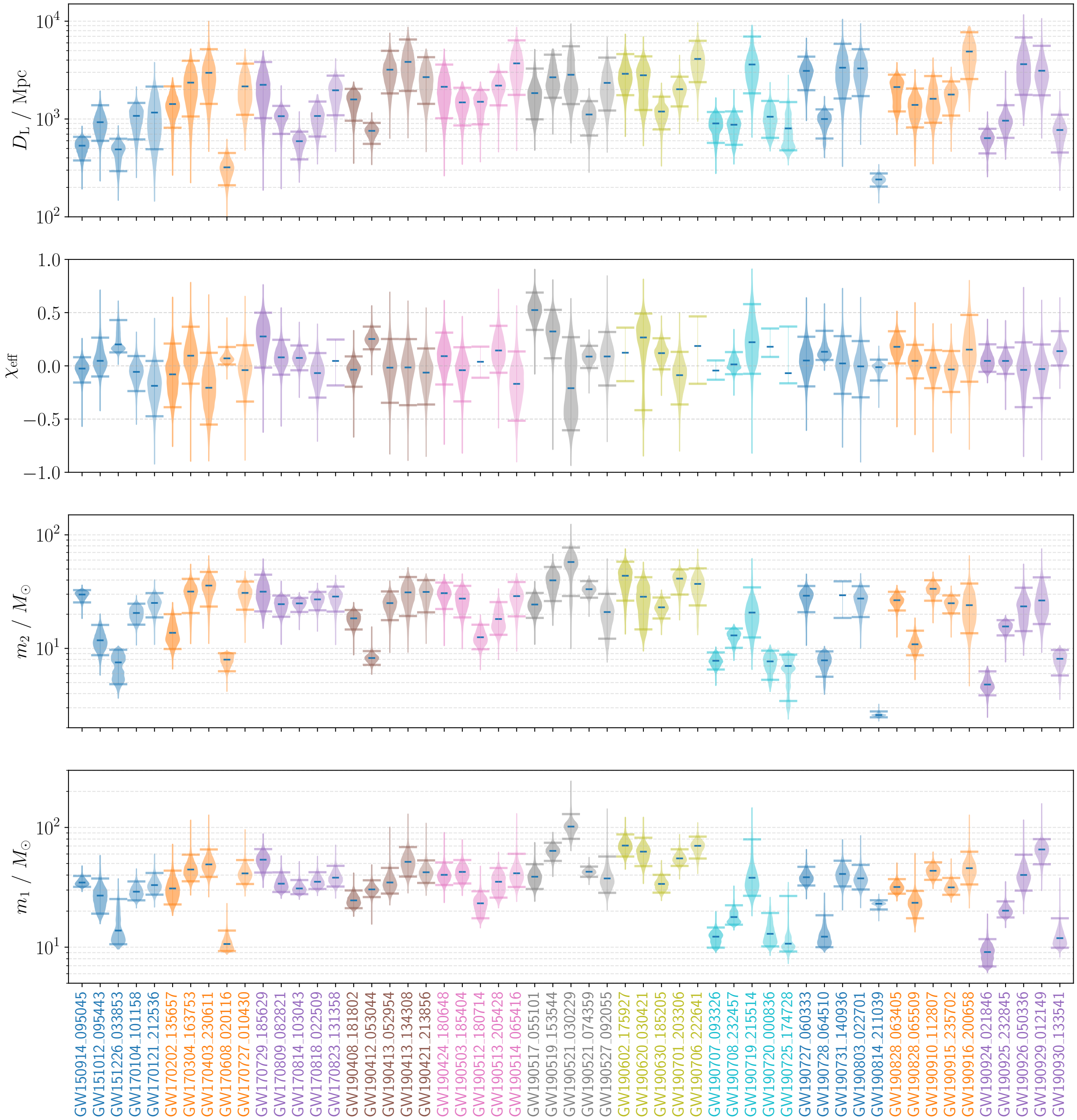

Figure 4. The marginalized distributions for component masses m_1, m_2, the effective spin $\chi_{\rm eff}$ and the luminosity distance $D_{\rm L}$ for all BBH events detected in 3-OGC. The median value, the 5th and 95th quantile values are marked with a bar, respectively. Different colors are used to aid associating each event with its posterior estimates.

making it either the least massive black hole or the most massive neutron star ever detected. If it is a neutron star, it should have a non-zero (albeit small) tidal deformability. Unfortunately, the signal-to-noise ratio of the event is not large enough to bound the tidal deformability away from zero, making it ambiguous whether the object was a neutron star or a black hole (Abbott et al. 2020e). These two events were also the first to have measurable power in sub-dominant harmonics, the $(l, m) = (3, 3)$ mode for both (Abbott et al. 2020g,e), which can be used to test general relativity as in Capano & Nitz (2020).

5.2. *Neutron Star Binaries*

The only observed neutron star binaries remain the previously reported GW170817 (Abbott et al. 2017a) and GW190425 (Abbott et al. 2020a). The latter is ob-

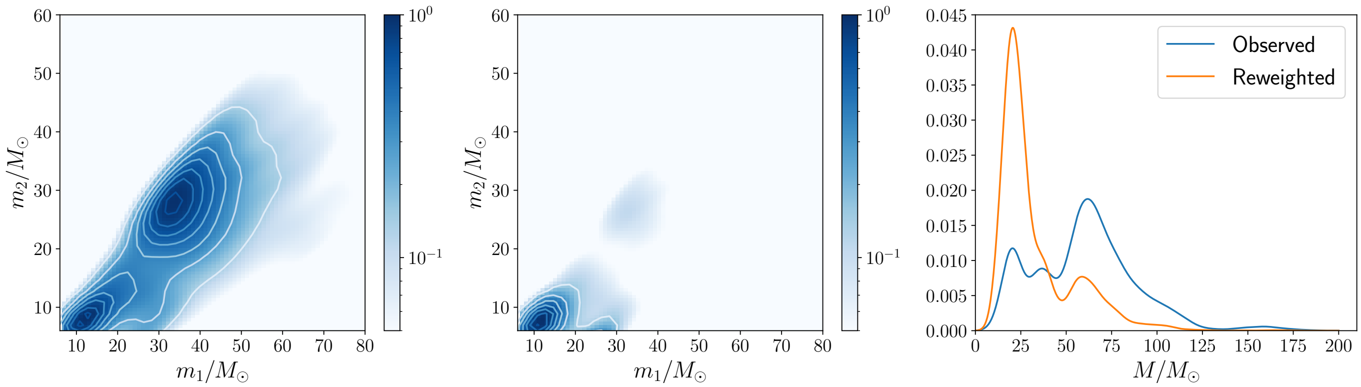

Figure 5. Distribution of the source-frame masses of the BBH population from the posteriors obtained from parameter estimation run on all detected BBH events. Here we show detected component mass distribution (left), component mass distribution corrected for the zeroth order selection effect (middle), and the one-dimensional marginals of the total mass distribution (right). The middle plot assumes a constant detection threshold and corrects the distribution for the effect of the signal loudness varying with component mass.

served in only the LIGO Livingston data, but given its separation from background, and the long duration of the signal which increases the power of signal consistency tests (Usman et al. 2016), we consider this detection robust. We obtain a slightly higher estimate for the effective spin of GW190425 than what was reported in (Abbott et al. 2020a). This can be attributed to a difference in prior: as stated above, we use a prior uniform in the spin-component aligned with the orbital angular momentum, whereas (Abbott et al. 2020a) used a prior on spin that was isotropic in orientation.

GW170817 is the only merger unambiguously observed by electromagnetic emission. Neutron star – black hole mergers have not yet been unambiguously observed. Due to the possibility of electromagentic emission from neutron star mergers, we encourage the use of sub-threshold BNS and NSBH candidates released with this catalog to investigate correlations with other archival observations and potentially detect faint sources.

5.3. *Sub-threshold Candidates*

In Table 3 we show the 17 sub-threshold candidates with $\mathcal{P}_{\rm astro} > 0.2$ or IFAR > 0.5. Several sub-threshold candidates have been previously identified. In particular, 151205_195525 was included in the 2-OGC catalog as a near threshold observation; in our updated analysis it is reduced in significance. 170425_055334 was previously reported in Venumadhav et al. (2019a). 151011_192749 was reported in 2-OGC as a sub-threshold event. The majority of these sub-threshold candidates are consistent with BBH mergers. However, 170722_065503 is consistent with a BNS merger. The full data release includes sub-threshold candidates at lower significance throughout the searched parameter space.

From visual inspection of time-frequency representations of the data around these candidates, there are no signs of loud noise transients that could have caused the corresponding triggers. In a few instances, minor excess power can be observed at frequencies between 50-100 Hz, or at lower frequencies. We cannot conclude if any of these minor power signatures correspond to an instrumental noise artefact or to a marginal astrophysical signal.

6. DATA RELEASE

We provide analysis configurations, metadata and results at https://github.com/gwastro/3-ogc (Nitz & Capano 2021b). The files contain $O(10^6)$ sub-threshold candidates along with their time, SNR, and values for various signal consistency tests. Each candidate event lists the associated false alarm rate and ranking statistic, to assess their significance. For the most significant candidates inside the focused BBH region discussed in section 3.2 we provide an estimate of the probability of astrophysical origin $\mathcal{P}_{\rm astro}$. We also release our Bayesian parameter inference posterior samples for each of the candidates shown in table 4 along with a selection of sub-threshold candidates. Additional data products and intermediate results may be made available upon request.

7. CONCLUSIONS

The 3-OGC catalog of gravitational-wave mergers covers the complete observing period from 2015 to 2019 and includes BNS, NSBH, and BBH candidates. For the first time we include candidates observed by a single sensitive detector. 3-OGC contains the most comprehensive set of merger candidates, including a total of 57 gravitational-wave observations in this period. This includes 4 single-detector mergers in addition to 4 BBH mergers reported here for the first time. We find no additional BNS or NSBH detections beyond the previously reported GW170817 and GW190425. Only the first half of the O3 run which concluded in 2020 has been made public. As the data from the latter half of the observing run is not yet released, the catalog here covers only O1, O2, and O3a. We expect the second half of O3, O3b to be released in 6 months, at which point an updated catalog will be produced.

ACKNOWLEDGMENTS

We thank Bruce Allen and Duncan Brown for providing useful comments. We are grateful to the computing team from AEI Hannover for their significant technical support. MC acknowledges funding from the Natural Sciences and Engineering Research Council of Canada (NSERC). This research has made use of data from the Gravitational Wave Open Science Center (https://www.gw-openscience.org), a service of LIGO Laboratory, the LIGO Scientific Collaboration and the Virgo Collaboration. LIGO is funded by the U.S. National Science Foundation. Virgo is funded by the French Centre National de Recherche Scientifique (CNRS), the Italian Istituto Nazionale della Fisica Nucleare (INFN) and the Dutch Nikhef, with contributions by Polish and Hungarian institutes.

REFERENCES

Aasi, J., et al. 2015, Class. Quantum Grav., 32, 074001, doi: 10.1088/0264-9381/32/7/074001

Abadie, J., et al. 2012, Phys. Rev., D85, 082002, doi: 10.1103/PhysRevD.85.082002

Abbott, B., et al. 2009, PhRvD, 80, 047101

—. 2017a, Phys. Rev. Lett., 119, 161101, doi: 10.1103/PhysRevLett.119.161101

—. 2019a, Phys. Rev. Lett., 123, 161102, doi: 10.1103/PhysRevLett.123.161102

—. 2020a, Astrophys. J. Lett., 892, L3, doi: 10.3847/2041-8213/ab75f5

Abbott, B. P., et al. 2016, Phys. Rev., D93, 122003, doi: 10.1103/PhysRevD.93.122003

—. 2017b, Astrophys. J., 848, L12, doi: 10.3847/2041-8213/aa91c9

—. 2017c, Astrophys. J., 851, L35, doi: 10.3847/2041-8213/aa9f0c

—. 2019b, Phys. Rev. X, 9, 031040, doi: 10.1103/PhysRevX.9.031040

—. 2019c, Astrophys. J., 883, 149, doi: 10.3847/1538-4357/ab3c2d

Abbott, R., et al. 2020b. https://arxiv.org/abs/2010.14527

—. 2020c, Phys. Rev. Lett., 125, 101102, doi: 10.1103/PhysRevLett.125.101102

—. 2020d, Astrophys. J. Lett., 900, L13, doi: 10.3847/2041-8213/aba493

—. 2020e, Astrophys. J. Lett., 896, L44, doi: 10.3847/2041-8213/ab960f

—. 2020f. https://arxiv.org/abs/2010.14533

—. 2020g, Phys. Rev. D, 102, 043015, doi: 10.1103/PhysRevD.102.043015

Abbott, R., Abbott, T., Abraham, S., et al. 2021a, SoftwareX, 13, 100658, doi: https://doi.org/10.1016/j.softx.2021.100658

Abbott, R., et al. 2021b. https://arxiv.org/abs/2105.06384

Acernese, F., et al. 2015, Class. Quantum Grav., 32, 024001, doi: 10.1088/0264-9381/32/2/024001

—. 2018, Class. Quant. Grav., 35, 205004, doi: 10.1088/1361-6382/aadf1a

Ade, P. A. R., et al. 2015. https://arxiv.org/abs/1502.01589

Ajith, P., Fotopoulos, N., Privitera, S., Neunzert, A., & Weinstein, A. J. 2014, Phys. Rev. D, 89, 084041, doi: 10.1103/PhysRevD.89.084041

Allen, B. 2005, Phys. Rev. D, 71, 062001, doi: 10.1103/PhysRevD.71.062001

—. 2021. https://arxiv.org/abs/2102.11254

Allen, B., Anderson, W. G., Brady, P. R., Brown, D. A., & Creighton, J. D. E. 2012, Phys. Rev. D, 85, 122006, doi: 10.1103/PhysRevD.85.122006

Andreoni, I., et al. 2018. https://arxiv.org/abs/1812.03161

Babak, S., Biswas, R., Brady, P., et al. 2013, Phys. Rev. D, 87, 024033, doi: 10.1103/PhysRevD.87.024033

Bhattacharjee, D., Lecoeuche, Y., Karki, S., et al. 2021, Class. Quant. Grav., 38, 015009, doi: 10.1088/1361-6382/aba9ed

Biwer, C. M., Capano, C. D., De, S., et al. 2019, Publ. Astron. Soc. Pac., 131, 024503, doi: 10.1088/1538-3873/aaef0b

Blanchet, L. 2002, Living Rev. Rel., 5, 3

Boh é , A., et al. 2016. https://arxiv.org/abs/1611.03703

Brown, D. A. 2004, PhD thesis, University of Wisconsin–Milwaukee
Buikema, A., et al. 2020, Phys. Rev. D, 102, 062003, doi: 10.1103/PhysRevD.102.062003
Burns, E., et al. 2019, Astrophys. J., 871, 90, doi: 10.3847/1538-4357/aaf726
Capano, C., Pan, Y., & Buonanno, A. 2013. https://arxiv.org/abs/1311.1286
Capano, C. D., Cabero, M., Abedi, J., et al. 2021. https://arxiv.org/abs/2105.05238
Capano, C. D., & Nitz, A. H. 2020, Phys. Rev. D, 102, 124070, doi: 10.1103/PhysRevD.102.124070
Chia, H. S., Olsen, S., Roulet, J., et al. 2021, Boxing Day Surprise: Higher Multipoles and Orbital Precession in GW151226. https://arxiv.org/abs/2105.06486
Cornish, N. J. 2010. https://arxiv.org/abs/1007.4820
Countryman, S., Keivani, A., Bartos, I., et al. 2019. https://arxiv.org/abs/1901.05486
Dal Canton, T., & Harry, I. W. 2017. https://arxiv.org/abs/1705.01845
Davies, G. S., Dent, T., Tápai, M., et al. 2020, Phys. Rev. D, 102, 022004, doi: 10.1103/PhysRevD.102.022004
Davis, D., Massinger, T. J., Lundgren, A. P., et al. 2019, Class. Quant. Grav., 36, 055011, doi: 10.1088/1361-6382/ab01c5
Davis, D., et al. 2021. https://arxiv.org/abs/2101.11673
Dietrich, T., Bernuzzi, S., & Tichy, W. 2017, Phys. Rev. D, 96, 121501, doi: 10.1103/PhysRevD.96.121501
Dietrich, T., Khan, S., Dudi, R., et al. 2019, Phys. Rev. D, 99, 024029, doi: 10.1103/PhysRevD.99.024029
Droz, S., Knapp, D. J., Poisson, E., & Owen, B. J. 1999, PhRvD, 59, 124016
Edelman, B., Doctor, Z., & Farr, B. 2021. https://arxiv.org/abs/2104.07783
Estellés, H., et al. 2021. https://arxiv.org/abs/2105.06360
Estevez, D., Lagabbe, P., Masserot, A., et al. 2021, Class. Quant. Grav., 38, 075007, doi: 10.1088/1361-6382/abe2db
Estevez, D., Mours, B., Rolland, L., & Verkindt, D. 2019, Online h(t) reconstruction for Virgo O3 data: start of O3, Tech. Rep. VIR-0652B-19, Virgo
Farr, W. M., Gair, J. R., Mandel, I., & Cutler, C. 2015, Phys. Rev. D, 91, 023005, doi: 10.1103/PhysRevD.91.023005
Faye, G., Marsat, S., Blanchet, L., & Iyer, B. R. 2012, Class. Quant. Grav., 29, 175004, doi: 10.1088/0264-9381/29/17/175004
Finstad, D., & Brown, D. A. 2020, Astrophys. J. Lett., 905, L9, doi: 10.3847/2041-8213/abca9e
Flanagan, E. E., & Hinderer, T. 2008, Phys. Rev. D, 77, 021502, doi: 10.1103/PhysRevD.77.021502
Fragione, G., Loeb, A., & Rasio, F. A. 2020, Astrophys. J. Lett., 902, L26, doi: 10.3847/2041-8213/abbc0a
Gayathri, V., Healy, J., Lange, J., et al. 2020. https://arxiv.org/abs/2009.05461
Gerosa, D., & Fishbach, M. 2021. https://arxiv.org/abs/2105.03439
Graham, M., et al. 2020, Phys. Rev. Lett., 124, 251102, doi: 10.1103/PhysRevLett.124.251102
Harry, I., Calder ó n Bustillo, J., & Nitz, A. 2018, Phys. Rev. D, 97, 023004, doi: 10.1103/PhysRevD.97.023004
Harry, I., & Lundgren, A. 2021. https://arxiv.org/abs/2101.01091
Harry, I., Privitera, S., Boh é , A., & Buonanno, A. 2016, Phys. Rev. D, 94, 024012, doi: 10.1103/PhysRevD.94.024012
Harry, I. W., Allen, B., & Sathyaprakash, B. 2009, Phys. Rev. D, 80, 104014, doi: 10.1103/PhysRevD.80.104014
Higson, E., Handley, W., Hobson, M., & Lasenby, A. 2018, Statistics and Computing, 29, 891913, doi: 10.1007/s11222-018-9844-0
Husa, S., Khan, S., Hannam, M., et al. 2016, Phys. Rev. D, 93, 044006, doi: 10.1103/PhysRevD.93.044006
Khan, S., Husa, S., Hannam, M., et al. 2016a, Phys. Rev. D, 93, 044007, doi: 10.1103/PhysRevD.93.044007
—. 2016b, Phys. Rev. D, 93, 044007, doi: 10.1103/PhysRevD.93.044007
Kimball, C., et al. 2020. https://arxiv.org/abs/2011.05332
Klimenko, S., et al. 2008, Class. Quantum Grav., 25, 114029
—. 2016, Phys. Rev. D, 93, 042004, doi: 10.1103/PhysRevD.93.042004
Liu, B., & Lai, D. 2021, Mon. Not. Roy. Astron. Soc., 502, 2049, doi: 10.1093/mnras/stab178
Marchant, P., Renzo, M., Farmer, R., et al. 2019, Astrophys. J., 882, 36, doi: 10.3847/1538-4357/ab3426
Mateu-Lucena, M., Husa, S., Colleoni, M., et al. 2021, Adding harmonics to the interpretation of the black hole mergers of GWTC-1. https://arxiv.org/abs/2105.05960
McIsaac, C., Keitel, D., Collett, T., et al. 2020, Phys. Rev. D, 102, 084031, doi: 10.1103/PhysRevD.102.084031
Messick, C., Blackburn, K., Brady, P., et al. 2016. https://arxiv.org/abs/1604.04324
Mozzon, S., Nuttall, L. K., Lundgren, A., et al. 2020, Class. Quant. Grav., 37, 215014, doi: 10.1088/1361-6382/abac6c
Nitz, A. H. 2018, Class. Quant. Grav., 35, 035016, doi: 10.1088/1361-6382/aaa13d
Nitz, A. H., Capano, C., Nielsen, A. B., et al. 2019a, Astrophys. J., 872, 195, doi: 10.3847/1538-4357/ab0108

Nitz, A. H., & Capano, C. D. 2021a, Astrophys. J. Lett., 907, L9, doi: 10.3847/2041-8213/abccc5

Nitz, A. H., & Capano, C. e. a. 2021b, 3-OGC Open Gravitational-wave Catalog, www.github.com/gwastro/3-ogc, GitHub

Nitz, A. H., Dent, T., Dal Canton, T., Fairhurst, S., & Brown, D. A. 2017, Astrophys. J., 849, 118, doi: 10.3847/1538-4357/aa8f50

Nitz, A. H., Dent, T., Davies, G. S., & Harry, I. 2020, Astrophys. J., 897, 169, doi: 10.3847/1538-4357/ab96c7

Nitz, A. H., Lenon, A., & Brown, D. A. 2019b, Astrophys. J., 890, 1, doi: 10.3847/1538-4357/ab6611

Nitz, A. H., Nielsen, A. B., & Capano, C. D. 2019c, Astrophys. J. Lett., 876, L4, doi: 10.3847/2041-8213/ab18a1

Nitz, A. H., & Wang, Y.-F. 2021a. https://arxiv.org/abs/2102.00868

—. 2021b, Phys. Rev. Lett., 126, 021103, doi: 10.1103/PhysRevLett.126.021103

Nitz, A. H., Harry, I. W., Willis, J. L., et al. 2018, PyCBC Software, https://github.com/gwastro/pycbc, GitHub

Nitz, A. H., Dent, T., Davies, G. S., et al. 2019d, Astrophys. J., 891, 123, doi: 10.3847/1538-4357/ab733f

O'Shaughnessy, R., Kim, C., Kalogera, V., & Belczynski, K. 2008, ApJ, 672, 479, doi: 10.1086/523620

Pratten, G., et al. 2020. https://arxiv.org/abs/2004.06503

Ramos-Buades, A., Tiwari, S., Haney, M., & Husa, S. 2020, Phys. Rev. D, 102, 043005, doi: 10.1103/PhysRevD.102.043005

Rolland, L., Seglar-Arroyo, M., & Verkindt, D. 2019, Reprocessing of h(t) for the last two weeks of O3a, Tech. Rep. VIR-1201A-19, Virgo

Romero-Shaw, I. M., Lasky, P. D., Thrane, E., & Bustillo, J. C. 2020, Astrophys. J. Lett., 903, L5, doi: 10.3847/2041-8213/abbe26

Roulet, J., Venumadhav, T., Zackay, B., Dai, L., & Zaldarriaga, M. 2020, Phys. Rev. D, 102, 123022, doi: 10.1103/PhysRevD.102.123022

Sathyaprakash, B. S., & Dhurandhar, S. V. 1991, Phys. Rev. D, 44, 3819, doi: 10.1103/PhysRevD.44.3819

Setzer, C. N., Biswas, R., Peiris, H. V., et al. 2018, doi: 10.1093/mnras/stz506

Skilling, J. 2006, Bayesian Analysis, 1, 833 , doi: 10.1214/06-BA127

Speagle, J. S. 2020, Monthly Notices of the Royal Astronomical Society, 493, 3132, doi: 10.1093/mnras/staa278

Stevenson, S., Ohme, F., & Fairhurst, S. 2015, ApJ, 810, 58, doi: 10.1088/0004-637X/810/1/58

Stevenson, S., Sampson, M., Powell, J., et al. 2019, doi: 10.3847/1538-4357/ab3981

Taracchini, A., Buonanno, A., Pan, Y., et al. 2014, PhRvD, 89, 061502, doi: 10.1103/PhysRevD.89.061502

Tiwari, V., et al. 2016, Phys. Rev. D, 93, 043007, doi: 10.1103/PhysRevD.93.043007

Usman, S. A., et al. 2016, Class. Quant. Grav., 33, 215004, doi: 10.1088/0264-9381/33/21/215004

Vajente, G., Huang, Y., Isi, M., et al. 2020, Phys. Rev. D, 101, 042003, doi: 10.1103/PhysRevD.101.042003

Vallisneri, M., Kanner, J., Williams, R., Weinstein, A., & Stephens, B. 2015, J. Phys. Conf. Ser., 610, 012021, doi: 10.1088/1742-6596/610/1/012021

van Son, L., de Mink, S., Broekgaarden, F., et al. 2020, Astrophys. J., 897, 100, doi: 10.3847/1538-4357/ab9809

Venumadhav, T., Zackay, B., Roulet, J., Dai, L., & Zaldarriaga, M. 2019a. https://arxiv.org/abs/1904.07214

—. 2019b, Phys. Rev. D, 100, 023011, doi: 10.1103/PhysRevD.100.023011

Viets, A., et al. 2018, Class. Quant. Grav., 35, 095015, doi: 10.1088/1361-6382/aab658

Wang, Y.-F., & Nitz, A. H. 2021, Astrophys. J., 912, 53, doi: 10.3847/1538-4357/abe939

Woosley, S. E. 2017, Astrophys. J., 836, 244, doi: 10.3847/1538-4357/836/2/244

Zackay, B., Dai, L., & Venumadhav, T. 2018, Relative Binning and Fast Likelihood Evaluation for Gravitational Wave Parameter Estimation. https://arxiv.org/abs/1806.08792

Zevin, M., Bavera, S. S., Berry, C. P. L., et al. 2021, Astrophys. J., 910, 152, doi: 10.3847/1538-4357/abe40e